

RETRO: Retroreflector Based Visible Light Indoor Localization for Real-time Tracking of IoT Devices

Sihua Shao

New Jersey Institute of Technology
ss2536@njit.edu

Abdallah Khreishah

New Jersey Institute of Technology
abdallah@njit.edu

Issa Khalil

Qatar Computing Research Institute
ikhail@qf.org.qa

Abstract—Indoor localization is very important to enable Internet-of-things (IoT) applications. Visible light communication (VLC)-based indoor localization approaches enjoy many advantages, such as utilization of existing ubiquitous lighting infrastructure, high location and orientation accuracy, and no interruption to RF-based devices. However, existing VLC-based localization methods lack a real-time backward channel from the device to landmarks and necessitate computation at the device, which make them unsuitable for real-time tracking of small IoT devices. In this paper, we propose and prototype a retroreflector-based visible light localization system (RETRO), that establishes an almost zero-delay backward channel using a retroreflector to reflect light back to its source. RETRO localizes passive IoT devices without requiring computation and heavy sensing (e.g., camera) at the devices. Multiple photodiodes (i.e., landmarks) are mounted on any single unmodified light source to sense the retroreflected optical signal (i.e., location signature). We theoretically derive a closed-form expression for the reflected optical power related to the location and orientation of the retroreflector, and validate the theory by experiments. The characterization of received optical power is applied to a received signal strength indicator and trilateration based localization algorithm. Extensive experiments demonstrate centimeter-level location accuracy and single-digit angular error.

Index Terms—Indoor localization, retroreflector, visible light.

I. INTRODUCTION

Indoor localization is an important field of application for Internet-of-Things (IoT), for example in warehouses, airports, railway stations, shopping centers, trade fairs, hospitals, offices and factories. Server-based indoor localization, which is suitable for asset and personal tracking, requires the device to send unique identity information to specific hardware, which can capture the information and forward them to a server to calculate the device's position. Real-time locating system (RTLS) is a typical field of application of server-based indoor localization. RTLS is used to automatically identify and track the location of objects or people in real time. Applications of RTLS include but are not limited to locating assets in a facility, such as tracking of medical instruments at a clinic, vehicles in industrial facilities and goods in retail shops; locating people, such as providing details about visitor flows, employer checking the current position of employees, and locating customers in a restaurant for food delivery.

Visible light communication (VLC) or LiFi [1] can be used as a localization technology [2]–[7]. LED or fluorescent lamps send out imperceptible flickering light that can be captured by a smart phone camera or photodetector. The information of received optical signal strength, angle-of-arrival, polarization and light distribution patterns can be leveraged for locating light sensing enabled devices. Relying on extensively and

homogeneously deployed lighting infrastructure, VLC-based localization approaches only require low-cost additional light source driver [2], [3], [7], or even do not need additional hardware [5], [6]. Thanks to the dominant line-of-sight (LOS) signal and incidence angle sensitive propagation path loss property, VLC-based localization can easily achieve sub-meter accuracy and also detect the orientation of devices [3]. Although VLC-based localization embraces many advantages, the absence of a real-time backward channel from devices to APs leads to impractical requirement of computation or heavy sensing (e.g., camera) on small IoT devices. Autonomously sending location and orientation information to the server results in inevitable latency to real-time tracking as well as unnecessary burden on IoT devices.

To address the above problems, which make conventional VLC-based approaches unsuitable for RTLS of passive IoT devices, we propose and prototype a retroreflector-based visible light localization system that we name RETRO. The retroreflector is a light-weight small device, which is capable of reflecting light back to its source with minimal scattering. Therefore, by mounting small-size light sensors, such as photodiodes (PDs), on infrastructural lamps, we can establish a backward channel from the retroreflector to VLC APs (i.e., lamps). In order to send unique identity information to APs, we add a liquid crystal display (LCD) shutter, which consumes only tens of μW with its driver circuit [8], [9], on the retroreflector to modulate and distinguish the reflected light for different IoT devices. The light-weight retroreflector along with an LCD shutter and its control unit can be installed on a passive IoT device to execute VLC-based real-time localization. The retroreflector can be realized by corner-cube, retroreflective sheeting [10] or even retroreflective spray paint [11]. In this work, we mainly study the corner-cube retroreflector. RETRO enjoys not only all the advantages (e.g., especially high location accuracy) provided by conventional VLC-based localization approaches, but also four unique and superior features: 1) RETRO can be implemented on any single unmodified light source; 2) immediate feedback from the retroreflector minimizes the latency of a centralized control of IoT devices; 3) RETRO is capable of localizing passive IoT devices with ultra-low power and no computational capability at the devices; 4) RETRO establishes a visible light uplink channel, which makes joint localization and communication without an additional uplink RF channel possible. In this paper, we utilize the received signal strength indicator (RSSI) and trilateration based localization algorithm (Sec. IV) to locate the retroreflector. The RSSI resulted from the retroreflected light is

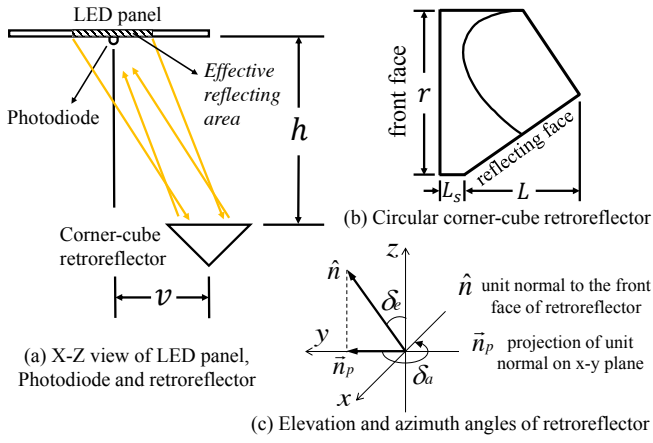


Fig. 1: Illustration of system parameters

theoretically analyzed (Sec. III) and experimentally validated (Sec. V). Based on experimental evaluation (Sec. VI), our proposed RETRO system can achieve centimeter-level localization accuracy and single-digit angular error.

In summary, we make three key contributions:

- To the best of our knowledge, RETRO is the first system that enables real-time tracking using the VLC-based localization approach. Relying on *any single unmodified* light source, RETRO is capable of localizing passive IoT devices without requiring computation or specialized hardware on the IoT device with minimum latency.
- We theoretically derive a closed-form expression for estimating retroreflected optical power from retroreflectors under Lambertian light source and experimentally validate the theory. Experimental results match theoretical results very well w.r.t different locations and orientations of the retroreflector.
- Based on the characterization of received optical power from the retroreflector, we develop an RSSI and trilateration based localization algorithm. We perform extensive experiments to evaluate the location and orientation accuracy of our proposed RETRO system and observe centimeter-level location accuracy (i.e., location error within 4.5 cm with the height of 1.5 meters) and up to 1° orientation error.

II. OVERVIEW OF THE LOCALIZATION APPROACH

In this work, RSSI and trilateration based localization approach [2] is used to estimate the position and orientation of an IoT device equipped with a retroreflector in the global frame of reference. Multiple PDs (i.e., landmarks) are mounted on one light source or multiple light sources to sense the reflected optical signal strength from a retroreflector. An LCD shutter (Sec. VI-A) covering the front face of retroreflector produces unique signal frequency for each retroreflector to distinguish the reflected light from multiple IoT devices and from environmental reflections. As the retroreflector changes its location and orientation, the received signal strength of each PD varies correspondingly. In order to investigate the relationship between the location and orientation of the retroreflector

and the received signal strength of each PD, we need to not only use the free space optical propagation model, but also characterize the area of light source, from which the light rays are retroreflected back to the corresponding PD. We call this area the *effective reflecting area*. In the next section, we theoretically study the effective reflecting area w.r.t different locations and orientations of the retroreflector.

III. ANALYSIS FOR RECEIVED OPTICAL POWER

A. System parameters

To derive the closed-form expression of retroreflected optical power, we define the following system parameters: 1. semi-angle at half power of light source, $\psi_{1/2}$. 2. refractive index of coating material of retroreflector, n . 3. length of retroreflector, L . 4. recessed length of retroreflector, L_s . 5. diameter of retroreflector's front face, r . 6. effective sensing area of PD, A_s . 7. transmitted optical power multiplied by reflector loss (reflector loss includes the transmission loss of the coating material and the reflection loss of each reflection surface), P_t . 8. Lambertian index, ml . 9. vertical distance between light source plane and the front face of retroreflector, h . 10. horizontal distance between the PD and the retroreflector, v . 11. elevation angle of the front face of the retroreflector, δ_e . 12. azimuth angle of the front face of the retroreflector, δ_a . The parameters are illustrated in Fig. 1.

To make the derivation clearer, we divide it into two steps: in the first step we consider a special case where the elevation and azimuth angles are both zero, and we analyze the boundary of the effective reflecting area based on the symmetry property of the incident and retroreflected rays; in the second step we study the other case where the elevation and azimuth angles are arbitrary, and since the derivation in case 1 cannot be simply applied to case 2, we create a virtual light source plane and utilize oblique projection to analyze the boundary of effective reflecting area. Note that the light source we consider here is a flat LED panel with evenly distributed light across the face of the panel. The derivation can be extended to the case where unevenly distributed light sources are considered.

B. Zero elevation and azimuth angles case

The distance between the PD and the retroreflector is

$$d = \sqrt{h^2 + v^2}. \quad (1)$$

Consider the scenarios when the distance between the light source and the retroreflector is much larger than the size of retroreflector, the radiance angles of all rays that are going to be reflected back to the PD can be approximated to be the same. Also, since the rays are reflected back along a vector that is parallel to but opposite in direction from the rays' source, the incidence angle to the PD is the same as the radiance angle. The value of radiance and incidence angles is

$$\theta = \tan^{-1} \frac{v}{h}. \quad (2)$$

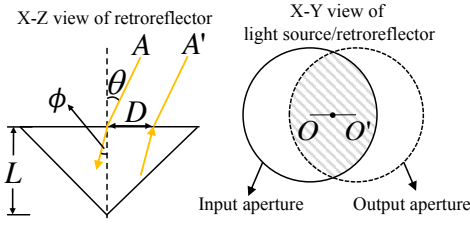


Fig. 2: Displacement of input and output apertures caused by the oblique angle of incidence to the retroreflector

According to Snell's law, the refracted angle is

$$\phi = \sin^{-1} \frac{\sin \theta}{n}. \quad (3)$$

As shown in Fig. 2, ray A incident on the center of the front face is retroreflected as ray A' . The points of intersection of A and A' with the front face are separated by D . Note that if $\theta = 0$, then $D = 0$. The solid line (circle O), which is the shape of the retroreflector face, is called the input aperture, and the dotted line (circle O'), which is giving the outline of the retroreflected beam, is the output aperture. We have $\overline{OO'} = D$. The intersection of the input and output apertures is the active reflecting area [12]. Assume a set of parallel rays incident on the front face of the retroreflector with angle θ , due to the symmetry of the incident and reflected rays requiring the last reflection to occur at a point inside the corner cube ([12] Page 9), only those within the active reflecting area are retroreflected. Note that in [12], the active reflecting area is given on the plane of the front face of the retroreflector to analyze the proportion of incident laser beam (i.e., a set of parallel light rays) that can be retroreflected. The theoretical analysis in [12] cannot be directly applied to Lambertian light source, from which the emitted light rays are not parallel. Therefore, in this paper, we utilize the concept of active reflecting area, as illustrated in Fig. 2, on the *plane of light source*. Assume a set of parallel rays incident on the front face of retroreflector with angle θ are emitted from the area within circle O on the light source plane, then only the rays from the intersection of circle O and O' are retroreflected. According to [12] (Page 10), the displacement of input and output apertures caused by the incidence angle θ is

$$D = 2L \tan \phi. \quad (4)$$

As shown in Fig. 3, the recession wall shadows the front face of the retroreflector at an oblique incidence angle. The recession leads to additional displacement of input and output apertures D_s ([12] Page 14). From the top view of the light source, the distance between circle O and circle O' is further increased by D_s . Therefore, the active reflecting area on the plane of the light source is further reduced due to recession. The displacement of input and output apertures caused by recession is ([12] Page 14)

$$D_s = 2L_s \tan \phi. \quad (5)$$

Given the displacements D and D_s , now we study which light rays are reflected to the PD. As shown in Fig. 4, V is

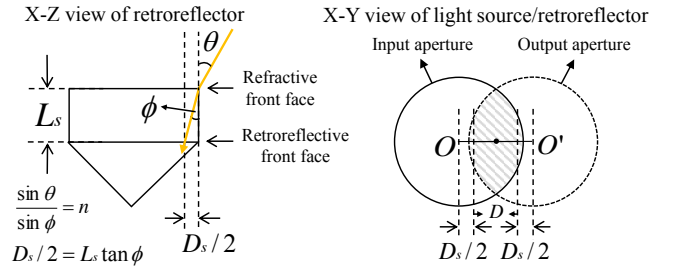


Fig. 3: Displacement of input and output apertures caused by the recession

the midpoint of $\overline{OO'}$, where $\overline{OO'} = D + D_s$. Recall that the shaded area contains a set of parallel rays, of which the incidence angles to the front face of the retroreflector are all θ , and this set of parallel rays can be retroreflected back to the shaded area. Suppose a ray from point P' is one of the parallel rays, the retroreflected ray intersects with the shaded area at point P , which is an equal distance on the other side of vertex V ([12] Page 9). Therefore, if P is where the PD is located at, and considering the parallel rays (radiance angles are all θ) from circle O , the ray from point P' is the one that can be retroreflected to the PD.

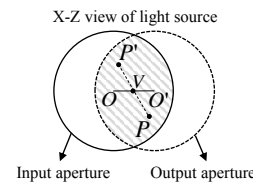


Fig. 4: Symmetry of incident ray and retroreflected ray

On the light source plane, there are uncountable small circles with the same size as that of circle O . Each small circle contains a set of parallel rays, whose radiance angle depends on the location of the corresponding small circle. If the PD is located in the shaded area of a small circle, in the corresponding set of parallel radiant rays, there exists a ray that can be reflected back to the PD. Therefore, there is an uncountable set of small circles, in each of them there exists a ray that can be reflected back to the PD. The intersection of the set of rays that can be reflected back to the PD with the *plane of light source* is the *effective reflecting area*.

Theorem 1: If the incidence angles of the light rays that can be retroreflected to the PD are approximated to be the same as the radiance angle θ , given two displacements D and D_s , and the diameter of retroreflector r , the size of effective reflecting area is the intersection of two circles, of which the radii are r and the distance between them is $2(D + D_s)$.

Proof: In order to evaluate the size of the effective reflecting area, we need to figure out its boundary. Consider a special case in Fig. 4, where P is on circle O , P' will be located on circle O' due to symmetry. It can be proved that for each point P'_m on $\overline{PP'}$ there exists a circle O and a circle O' , where the intersection of two circles includes both P'_m and P , and the symmetry in Fig. 4 holds. Therefore, for every point on $\overline{PP'}$ there exists a ray that can be retroreflected to P . P' is the furthest point (from which there exists a ray that can be retroreflected to P) away from P along the direction of $\overrightarrow{PP'}$. Since the incidence angles of the light rays that can be retroreflected to the PD are approximated to be the same,

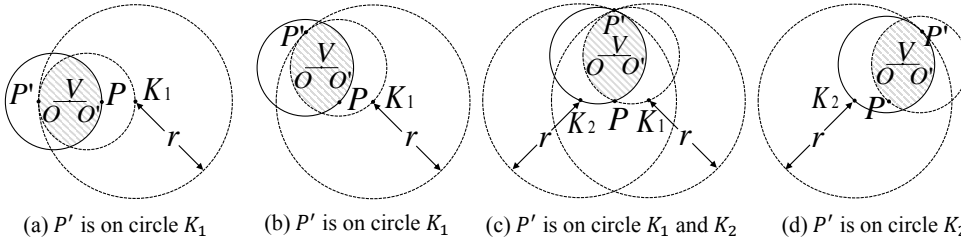


Fig. 5: Four cases when using symmetry of incident ray and retroreflected ray to analyze the boundary of effective reflecting area

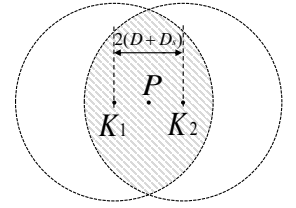


Fig. 6: Effective reflecting area

the separation distances and directions of circle O' for all the possible locations of circle O are the same. Therefore, if we rotate the intersection of circle O and circle O' (i.e., the shaded area in Fig. 4) around P and keep P on the boundary of the intersection, considering P as the location of PD, the trajectory of P' will be the boundary of the effective reflecting area.

In Fig. 5, we use two big circles (K_1 and K_2), of which the radii are r (i.e., diameter of circle O), to analyze the trajectory of P' . The distance $\overline{PK_1}$ and $\overline{PK_2}$ are both equal to $\overline{OO'}$, and both $\overline{PK_1}$ and $\overline{PK_2}$ are parallel to $\overline{OO'}$. In Fig. 5 (a), $\angle P'K_1P = 0^\circ$, since $\overline{PP'} = r - \overline{OO'}$ and $\overline{PK_1} = \overline{OO'}$, $\overline{P'K_1} = r$ which indicates that P' is on circle K_1 . In Figs. 5 (b), (c) and (d), it can be proved by the similarity between $\triangle P'VO'$ and $\triangle P'PK_1$ (or $\triangle P'VO$ and $\triangle P'PK_2$) that $\overline{P'K_1} = r$ (or $\overline{P'K_2} = r$), which indicates that P' is either on circle K_1 or on circle K_2 when we rotate the intersection of circle O and O' (i.e., the shaded area in Fig. 5) around P and keep P on the intersection boundary. Therefore, the trajectory of P' is the boundary of the intersection of circle K_1 and K_2 . The effective reflecting area is the shaded area in Fig. 6. ■

Given D and D_s , the ratio of effective reflecting area to the maximum effective reflecting area (i.e., when $D + D_s = 0$) is

$$\alpha = \frac{2r^2(\cos^{-1} \frac{D+D_s}{r} - \frac{D+D_s}{r} \sin(\cos^{-1} \frac{D+D_s}{r}))}{\pi r^2}. \quad (6)$$

Since the radiance angle of the effective reflecting area is equal to the incidence angle to the PD and the propagation distance is $2d$, according to the free space optical path loss model in [13], the received optical power is

$$P_r = P_t \frac{(ml + 1)A_s}{8\pi d^2} \cos^{ml+1} \theta \alpha. \quad (7)$$

C. Arbitrary value of elevation and azimuth angles case

If the front face of the retroreflector is not parallel to the light source plane, we cannot directly apply the analysis in case 1 (i.e., when $\delta_e = 0$ and $\delta_a = 0$) by simply varying the incidence angle to the front face of retroreflector. This is because the shape of the front face of retroreflector is different from its oblique projection along the direction of retroreflected light rays on the light source plane.

As shown in Fig. 7, the retroreflector plane is parallel to the light source plane. Point P is where the PD is located at. Point P' is the projection of P on the retroreflector plane. Point O is the center of the front face of retroreflector. We use $\overline{P'O}$ as the direction of y axis and form the 3D coordinate systems for both the retroreflector and the light source. If the

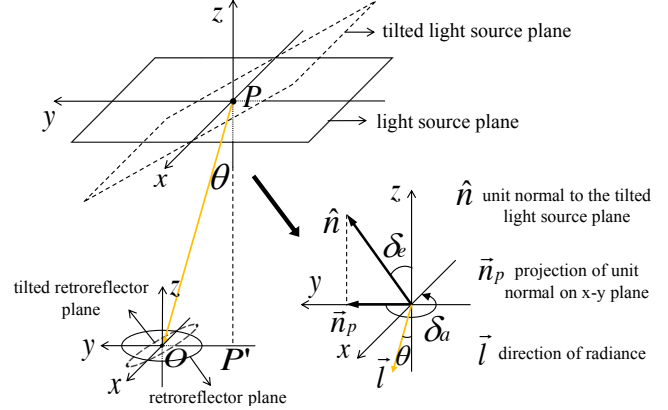


Fig. 7: A virtual light source plane to illustrate Theorem 2

retroreflector changes its orientation and its front face is on a tilted retroreflector plane, we create a virtual tilted light source plane, which is parallel to the tilted retroreflector plane. The intersection line of the real light source plane and the virtual tilted light source plane crosses point P . Now we can perform the same analysis in case 1 (i.e., when $\delta_e = 0$ and $\delta_a = 0$) on the tilted light source plane based on the new incidence angle to the front face of tilted retroreflector, which is formed by the normal \hat{n} to the tilted retroreflector plane and \overline{OP} . Therefore, the size of a virtual effective reflecting area S on the tilted light source plane can be derived from (6).

The virtual effective reflecting area S on the tilted light source plane contains a set of rays that can be retroreflected back to the PD. These rays are approximated to be parallel to \overline{PO} . In order to figure out the effective reflecting area S' on the real light source plane, we need to derive the oblique projection of S on the real light source plane along the direction of \overline{PO} . As shown in Fig. 7, in the coordinate system of light source, \hat{n} is the unit normal to the tilted light source plane, and \vec{n}_p is the projection of \hat{n} on x - y plane. Elevation angle δ_e is formed by \hat{n} and the z axis, azimuth angle δ_a is formed by \vec{n}_p and the y axis, \vec{l} denotes the direction of \overline{PO} , and radiance angle θ is formed by \vec{l} and the z axis.

Theorem 2: Given θ , δ_e and δ_a , the ratio of S' and S , β , is equal to $\cos \delta_e - \sin \delta_e \tan \theta \cos \delta_a$.

Proof: In Fig 8, point A is on the tilted light source plane, point A_p is the projection of point A on the real light source plane, and point A_{op} is the oblique projection of point A on the real light source plane along the direction of \vec{l} , where \overline{AP} , $\overline{A_pP}$ and $\overline{A_{op}P'}$ are all perpendicular to

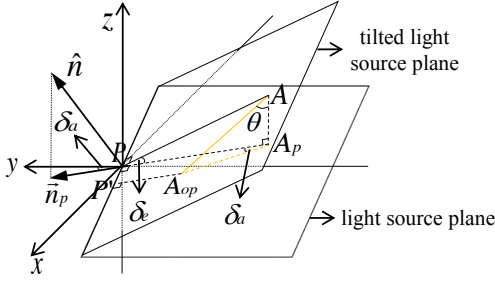


Fig. 8: Point A is on the tilted light source plane and its oblique projection A_{op} is on the light source plane

the intersection line of the real light source plane and the virtual tilted light source plane. The direction of $\overrightarrow{A_p P}$ is the same as that of $\overrightarrow{n_p}$. Therefore, $\angle APA_p = \delta_e$, $\angle A_{op} AA_p = \theta$, $\angle PA_p A_{op} = \delta_a$. It can be proved by the principle of calculus that $\frac{S'}{S} = \frac{A_{op} P'}{AP}$. Since $\overrightarrow{A_p P} = \overrightarrow{AP} \cos \delta_e$, $\overrightarrow{A_p A_{op}} = \overrightarrow{AA_p} \tan \theta = \overrightarrow{AP} \sin \delta_e \tan \theta$ and $\overrightarrow{A_{op} P'} = \overrightarrow{A_p P} - \overrightarrow{A_p A_{op}} \cos \delta_a = \overrightarrow{AP} \cos \delta_e - \overrightarrow{AP} \sin \delta_e \tan \theta \cos \delta_a$, we have

$$\beta = \frac{S'}{S} = \frac{A_{op} P'}{AP} = \frac{\overrightarrow{AP} \cos \delta_e - \overrightarrow{AP} \sin \delta_e \tan \theta \cos \delta_a}{\overrightarrow{AP}} \quad (8)$$

Substituting the incidence angle to the front face of the tilted retroreflector (i.e., formed by the normal \hat{n} to the tilted retroreflector plane and \overrightarrow{OP} in Fig. 7) to (4) and (5), we can find D and D_s for the tilted retroreflector. Substituting D and D_s for the tilted retroreflector to (6), we can find the ratio of the effective reflecting area and the maximum effective reflecting area α on the virtual tilted light source plane. Therefore, the received optical power

$$P_r = P_t \frac{(ml+1)A_s}{8\pi d^2} \cos^{ml+1} \theta \alpha \beta. \quad (9)$$

D. Practical concern

In practice, the retroreflector may not rotate around the center of its front face. As shown in Fig. 9, the distance between the front face of the retroreflector and the rotation center is R . Therefore, the new vertical distance between the light source and the retroreflector is $h_{new} = h + R(1 - \cos \delta_e)$. The new horizontal distance between the PD and the retroreflector is

$$\begin{aligned} v_{new} &= \overrightarrow{O'P} = \sqrt{(\overrightarrow{OP} + \overrightarrow{OO'} \cos \delta_a)^2 + (\overrightarrow{OO'} \sin \delta_a)^2} \\ &= \sqrt{(v + R \sin \delta_e \cos \delta_a)^2 + (R \sin \delta_e \sin \delta_a)^2} \end{aligned}$$

In order to recompute P_r in (9), we substitute h_{new} and v_{new} into (1)-(6) and (8), and get the new values of d , θ , α and β .

IV. LOCALIZATION ALGORITHM

Given n PDs mounted on the light source plane, we can apply (9) to form constraints on measured received optical power and distances between the PDs and the retroreflector, as well as the azimuth and elevation angles of the retroreflector,

$$P_{ri} = P_t \frac{(ml+1)A_{si}}{8\pi d_i^2} \cos^{ml+1} \theta_i \alpha_i \beta_i, i = 1, 2, \dots, n. \quad (10)$$

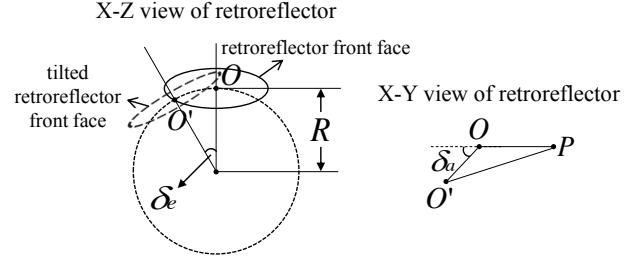


Fig. 9: When rotation center is not coincident with the center of the front face of retroreflector

Let the 3D coordinates of the retroreflector and the i -th PD be (x_0, y_0, z_0) and (x_i, y_i, z_i) , respectively. We have the horizontal distance between the i -th PD and the retroreflector $v_i = \sqrt{(x_0 - x_i)^2 + (y_0 - y_i)^2}$ and the vertical distance between the light source plane and the front face of the retroreflector $h = |z_0 - z_i|$. Recall that the azimuth and elevation angles of the retroreflector are denoted by δ_a and δ_e , respectively. Therefore, there are five unknowns x_0, y_0, z_0, δ_a and δ_e when we estimate the position and orientation of the retroreflector. With five or more PDs with known 3D coordinates, we can uniquely determine all the five unknowns. Note that since the landmarks in RETRO system are PDs instead of light sources (i.e., landmarks in conventional VLC-based localization approaches), RETRO is able to locate devices with *any single unmodified* light source. The localization is framed as an optimization process trying to minimize the sum of square errors between the left and right hand sides of (10),

$$\vec{s}_{opt} = \arg \min_s \sum_i f_i(\vec{s})^2,$$

where $\vec{s} = (x_0, y_0, z_0, \delta_a, \delta_e)$ and

$$f_i(\vec{s}) = P_{ri} - P_t \frac{(ml+1)A_{si}}{8\pi d_i^2} \cos^{ml+1} \theta_i \alpha_i \beta_i, i = 1, 2, \dots, n.$$

To accelerate the search process for the above non-linear least square optimization problem, the widely-used Levenberg-Marquardt algorithm [4] is adopted. Levenberg-Marquardt algorithm reduces the search space by searching along the direction of the gradient, which moves toward the local minimum. The initial values of unknowns are generated randomly and we run the localization algorithm several times to avoid local minima. The efficiency of the Levenberg-Marquardt algorithm is proved in [4], which can converge to a local minimum in several milliseconds. In our experiments, we show that the localization algorithm can generate very high location and orientation accuracy.

V. EXPERIMENT BASED VALIDATION OF THE DERIVATION OF RECEIVED OPTICAL POWER

A. Testbed settings

We utilize a flat LED panel with evenly distributed light as the light source, which is a commercial off-the-shelf (COTS) LED Troffer 2x2 FT (35W, 4000K, 3770 Lumens) provided by Hyperikon. To estimate $\psi_{1/2}$ of the LED panel, we

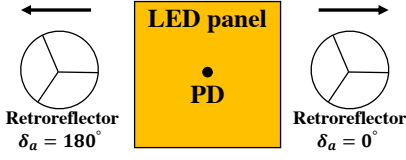


Fig. 11: Explanation of light leaking problem (only when $\delta_a = 0^\circ$, total internal reflection property holds when v increases)

manually restrict the effective illumination area to a small spot and find out that $\psi_{1/2} = 33^\circ$, and the Lambertian index $ml = -\frac{\ln 2}{\ln(\cos \psi_{1/2})}$. The circular retroreflector PS976 (uncoated) is manufactured by Thorlabs [14]. The substrate material is BK7 grade A, according to [15], with a refractive index $n = 1.51$ for visible light wavelength. According to [14], the length of retroreflector $L = 35.7 \text{ mm}$, the length of recession $L_s = 6.3 \text{ mm}$ and the diameter of the front face of retroreflector $r = 50 \text{ mm}$. The PD S6968 is provided by Hamamatsu Photonics [16], and $A_s = 150 \text{ mm}^2$. The value of P_t is estimated by fitting the measurements at different heights to the theoretical values.

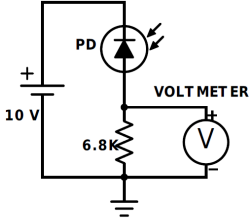


Fig. 10: Light intensity measurement circuit

The PD works in photoconductive mode to measure the light intensity. As shown in Fig. 10, the PD is driven by a 10 V DC and cascaded with a $6.8\text{k}\Omega$ resistor. The received optical power P_r is linearly proportional to the output voltage of the resistor, which is measured by a multimeter. To get rid of the environmental reflection, we use an opaque chip to cover the front face of the retroreflector and measure the output voltage generated by environmental reflection, then we remove the opaque chip to measure the amount of output voltage contributed by the reflection of the retroreflector. We fix the retroreflector on a tripod to perform measurements at different locations and orientations. The testbed is shown in Fig. 12.

B. Experiment results

When we perform the measurement of the received optical power without changing the orientation (i.e., zero-value elevation and azimuth angles), we keep the retroreflector at certain height and increase the horizontal distance between the PD and the retroreflector. We observe that the output voltage drops suddenly to zero at a certain horizontal distance when the azimuth angle is non-zero. As shown in Fig. 11, if the azimuth angle is 0° , as the horizontal distance increases, the output voltage decreases smoothly; while if the azimuth angle is 180° , the output voltage suddenly drops to zero when the horizontal distance increases to a certain value. This phenomenon contradicts the isotropic property of circular retroreflectors. After experimentally studying the retroreflector and communicating with the technical support from Thorlabs, we confirm that the reason for the an-isotropic phenomenon is due to the light leaking problem of the three mutually perpendicular reflecting surfaces. If the angle of incidence

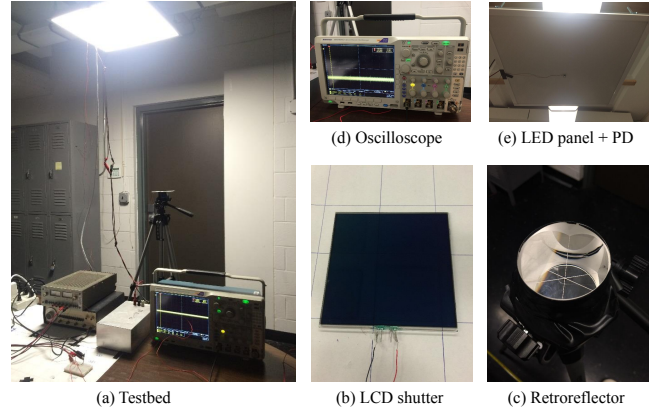


Fig. 12: Testbed

(AOI) to one of the three reflecting surfaces is too small, light will be leaking out of the surface instead of being reflected; thus, the total internal reflection (TIO) does not stand anymore. However, the light leaking problem is not a fundamental problem of retroreflectors and can be resolved by re-fabricating three reflecting surfaces to let them reflect as mirrors. Therefore, the isotropic property can hold such that the circular retroreflector is suitable for localization.

To circumvent the light leaking problem, we perform all the experiments at zero azimuth angle, in which case the AOI to each reflecting surface will not be small enough to cause light leaking. To validate the theory in case 1 (equation (7)), we measure the output voltage at 4 different heights; namely, 1 meter, 1.18 meters, 1.35 meters and 1.52 meters. For each height, the measurement is performed at horizontal distances from 0 cm to 90 cm at intervals of 2 cm. The results are shown in Fig. 13. To validate the theory in case 2 (equation (9)), we measure the output voltage at fixed height 1 meter and 4 different horizontal distances; namely, 0 cm, 10 cm, 20 cm and 30 cm. For each horizontal distance, the elevation angle δ_e is varied from 0° to 30° at intervals of 2° . The results are shown in Fig. 14. Since the experimental and the theoretical results match very well, we can safely conclude that the closed-form expression of received optical power is a very accurate approximation to practical measurements.

VI. EXPERIMENT BASED EVALUATION OF LOCALIZATION AND ORIENTATION ACCURACY

A. Applying LCD shutter

In practice, in order to distinguish the reflected light from multiple IoT devices and from environmental reflection, instead of passive opaque chip, an active LCD shutter can be used to cover the front face of retroreflector to modulate the retroreflected light [8], [9]. By transitioning between transparent and opaque states, LCD shutter can approximate a square wave signal at low modulation frequency. To investigate the relationship between signal amplitude and modulation frequency, we measure the signal amplitude by placing three types of LCD shutter (i.e., conventional, video and Pi-cell) between a small LED light bulb and a photodetector (PDA36A

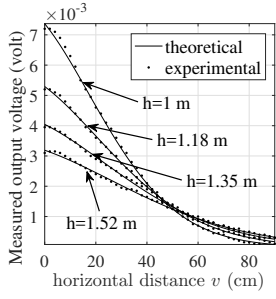


Fig. 13: Theoretical and experimental results of zero-value elevation and azimuth angles setting

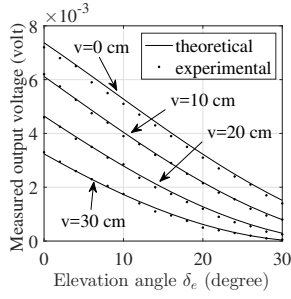


Fig. 14: Theoretical and experimental results of arbitrary-value elevation and azimuth angles setting

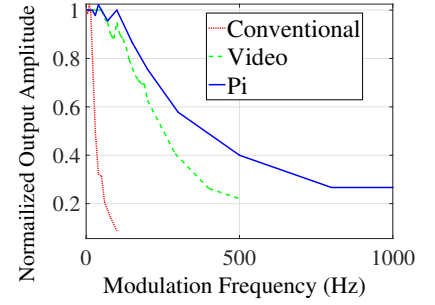


Fig. 15: Signal amplitude vs. modulation frequency for three types of LCD shutters

from Thorlabs). The results are shown in Fig. 15, it can be seen that the signal amplitude decreases quickly for all three types of LCD shutters. This is due to the long response time (i.e., time cost by transitioning from one state to the other) of LCD shutters. Therefore, we choose a low modulation frequency (20 Hz) to drive the LCD shutter. Different modulation frequencies can be utilized to drive different LCD shutters in order to support multiple access of IoT devices. The capacity of the system and the impact on localization accuracy of mutual interference among different devices will be studied in the future.

In our experiments, Pi-cell is selected as the modulator. It is driven by a function generator. Note that the power consumption of the LCD shutter and its driver circuit is at tens of μW , which is also validated in [8], [9]. Instead of connecting the light intensity measurement circuit to a multimeter, we connect it to an oscilloscope (Tektronix MDO4034-3) and set the sampling rate to 1 MS/s. The recorded data is processed in MATLAB through Fast Fourier Transform (FFT) to compute the signal amplitude. Denote the FFT length by N , the amplitude of the 1st harmonics in frequency domain by A_f and the amplitude of the square wave in time domain by A_t , we have $A_f = A_t/(N/2)$. In Fig. 16, we show the FFT plot including retroreflected optical signal (20 Hz) and background light (60 Hz). We can observe that the background noise is much less than the 20 Hz signal amplitude, which enables reliable signal amplitude estimation at the modulation frequency of LCD shutter.

Besides the modulation frequency, viewing angle also affects the amplitude of the signal produced by LCD shutter. We place the Pi-cell between a small light bulb and a photodetector (PDA36A from Thorlabs) at 8 values of azimuth angles (i.e., 0° , 45° , 90° , 135° , 180° , 225° , 270° and 315°) and 9 values of elevation angles (i.e., 0° , 5° , 10° , 15° , 20° , 25° , 30° , 35° and 40°) to measure the signal amplitude. The results are shown in Fig. 17. When the elevation angle is not larger than 30° , the variation of signal amplitudes for different azimuth angles is very small. However, when the elevation angle increases above 30° , the signal amplitudes at azimuth angles of 45° and 225° are much lower than those at other azimuth angles. Therefore, the isotropic property of circular retroreflector may not hold when the incidence angle to the front face of retroreflector is larger than 30° . This issue can be resolved by selecting

the closest PDs to perform localization, but it still restricts the orientation range to some extent. Another solution might be using dispersion film instead of LCD shutter, such that the viewing angle issue does not exist. However, the properties and limitations of dispersion film need to be studied thoroughly in the future. In Fig. 17, we can also observe that as the elevation angle of Pi-cell increases from 0° to 30° , the signal amplitude decreases. We use a linear function $\gamma(\theta) = 1 - 0.005\theta$ to approximate the attenuation caused by the viewing angle of Pi-cell, where θ is the incidence angle to the front face of the retroreflector. To compute the received optical power using (9), the right hand side of the equation needs be multiplied by γ^2 since the light rays pass through the Pi-cell twice.

B. Localization and orientation accuracy

Recall that the light leaking problem restricts all the received signal amplitude measurements at zero azimuth angle (Fig. 11). The problem can be handled by manufacturing a corner-cube with three reflecting surfaces as normal mirrors. However, we are using the COTS corner-cube retroreflector, which is designed for laser based applications. Due to the intrinsically isotropic property of circular corner-cube retroreflectors, the light leaking problem caused by laser application-oriented COTS product manufacturing does not hinder the evaluation of localization accuracy. We apply the measurement results using one PD to a realistic localization system, where multiple PDs are mounted on the LED panel in a grid structure with intervals of 20 cm. A central controller is used to monitor the signal amplitudes from all the PDs. Once the central controller detects the signal at certain frequency (20 Hz in our experiment), it selects the PD, whose output signal amplitude is the largest, as the central one and uses the other 4 PDs around the central one to perform the localization algorithm. As shown in Fig. 18, the area within the dashed-line square is the region in which we are evaluating the localization accuracy when the elevation and the azimuth angles of the retroreflector are both zero.

We select 400 positions uniformly within the dashed-line square region and compute the corresponding horizontal distances to each PD. Then we perform the signal amplitude measurement using one PD at all horizontal distances. After we measure the signal amplitudes at 4 different heights (75

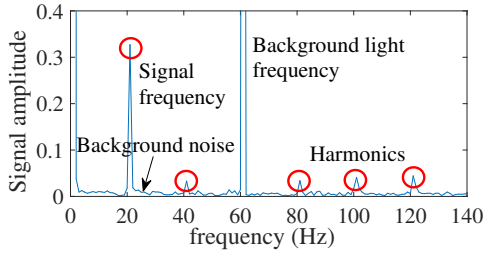


Fig. 16: FFT plot of received signal (low background noise)

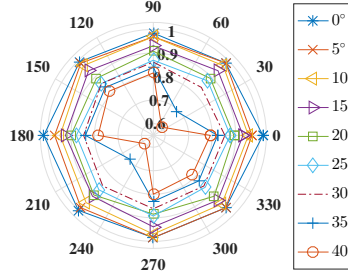


Fig. 17: Normalized signal amplitude vs. different viewing angles

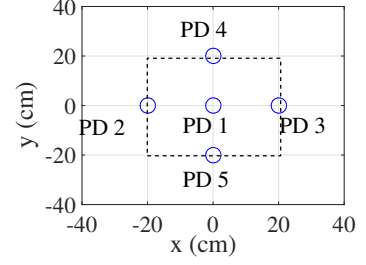


Fig. 18: XY view (top) of PDs in grid structure

cm, 1 m, 1.25 m and 1.5 m), we input them to the RSSI and trilateration based localization algorithm (Sec. IV) to evaluate the localization accuracy. In Fig. 19, we apply our algorithm for 3D localization, in which the height is unknown, and we can observe that, at the height of 1.5 m, the location errors are less than 6 cm in 90% of the cases and the median error is only 2 cm. In Fig 20, the height is known. At the height of 1.5 m, the location errors are less than 2 cm in 90% of the cases and the median error is only 1 cm.

To evaluate both the location and the orientation accuracy, due to the light leaking problem and viewing angle restriction, we only consider PD1, PD2 and PD3 in Fig. 18 to evaluate the elevation angle accuracy when the retroreflector is placed at (0,0) and (10,0) where the height is 1 meter. Note that the viewing angle restriction to valid orientation detection range might be resolved by utilizing dispersion film which needs to be investigated thoroughly, or by leveraging a gyroscope and sending the detected orientation information back to the tracking system via the uplink enabled by the retroreflector. We vary the elevation angle from -10° to 10° when the retroreflector is placed at (0,0) and vary the elevation angle from -5° to 5° when the retroreflector is placed at (10,0). In Fig 21, we apply our 3D localization algorithm, in which the height is unknown, 90% of the location errors are less than 12 cm, 80% of the angular errors are less than 6° , and the median location and angular errors are 3 cm and 2° , respectively. In Fig 22, the height is known, 80% of the location errors are less than 5 cm, 80% of the angular errors are less than 3° , and the median location and angular errors are 1 cm and 1° , respectively. As far as we know, in VLC-based localization systems, Luxapose [3] is the only system that both enables the tracking of devices' orientation and evaluates the orientation accuracy. In our 3D location and orientation results (Fig. 21), using simple and cheap PDs, we are able to achieve parity with the 2D location and orientation results (i.e., height is known) of systems such as Luxapose [3] that requires CMOS imager and heavy computation to obtain angle-of-arrival (AOA) information. In our 2D location and orientation results (Fig. 22), we are able to achieve 40% improvement in both location and orientation accuracy compared to Luxapose.

In Fig. 23, we only evaluate the orientation error from localization. Compared to Luxapose [3], in which the angle error is less than 3° when only orientation is evaluated, we

are able to achieve 60% improvement in terms of orientation accuracy. In addition, Luxapose [3] requires four or five customized light beacons to be visible for a camera to achieve decimeter-level location accuracy and roughly 3° orientation error. However, by relying on only one *single unmodified* light source, RETRO extends the available localization area, within which centimeter-level location accuracy and 1° orientation error can be achieved without requiring computation and heavy sensing, like camera, on the device.

VII. RELATED WORK

RF-based localization approaches. The localization accuracy (less than 1 meter) of RFID [17] depends on densely deployed RFID readers, which are very expensive. Utilizing existing infrastructure, WiFi-based localization [18], [19] can localize devices within large range. Although in the most recent WiFi-based localization works [18], [19], authors claim that the WiFi-based localization approach can achieve decimeter-level accuracy, the location error reaches to 2 meters at the 80th percentile, which can cause destructive outcome for some location error sensitive applications. Bluetooth low energy (BLE), such as iBeacon [20], is intrinsically low frequency radio (i.e., use the same spectrum as WiFi) and therefore, the location error can still reach to meter-level and the interference to WiFi-based user devices is considerable. Ultra-wideband (UWB)-based localization [21] is able to achieve location precision within tens of centimeters. Nevertheless, the high cost of hardware, shorter battery lifetime than BLE, and lack of interaction with the current devices render UWB-based localization not being used universally.

VLC-based localization approaches. Existing VLC based localization works are not suitable for real-time tracking of passive IoT devices not only because of the absence of backward channel. Epsilon [2] and Luxapose [3] require modified light infrastructure by adding extra driver circuit. Litell [5] requires specific unmodified light source like fluorescent lamp. Luxapose [3] and PIXEL [4] require a power-consuming camera facing upward to keep capturing images containing enough landmarks. Navilight [6] requires the object to move for a certain distance to collect light intensity pattern. Based on existing light infrastructure with any unmodified light source, RETRO is capable of determining the position and the orientation of any passive IoT devices with ultra-low power and no camera, expensive sensor, or computational capability at

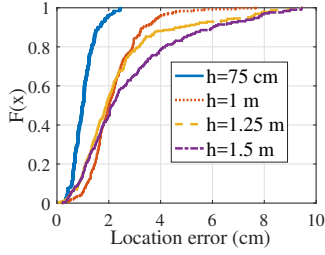


Fig. 19: Empirical CDF of 3D location error

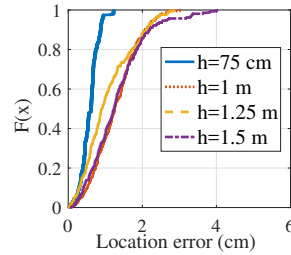


Fig. 20: Empirical CDF of 2D location error

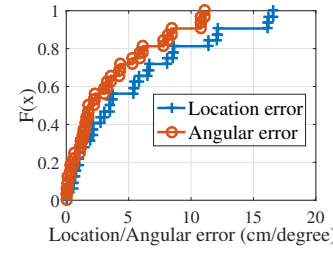


Fig. 21: Empirical CDF of 3D location and orientation error

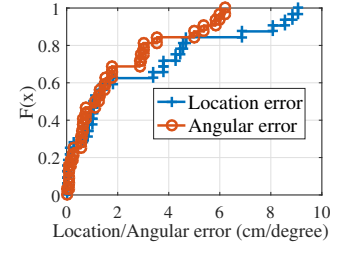


Fig. 22: Empirical CDF of 2D location and orientation error

System	Epsilon	Luxapose	PIXEL	Litell	Navilight	RETRO
Reference	[2]	[3]	[4]	[5]	[6]	[this]
Location accuracy (90%)	0.4 m	0.1 m	0.3 m	0.1 m	1 m	2 cm
Orientation accuracy	N/A	3°	N/E	N/A	N/A	1°
Method	Model	AoA	AoA	FP	FP	Model
Database	No	Yes	Yes	Yes	Yes	No
Unmodified infrastructure	No	No	Yes	Yes	Yes	Yes
Require multiple light sources	Yes	Yes	No	No	No	No
Require camera	No	Yes	Yes	Yes	Yes	No

TABLE I: Comparison with VLC-based localization systems. N/E stands for not evaluated. FP and AoA are fingerprinting and angle-of-arrival, respectively.

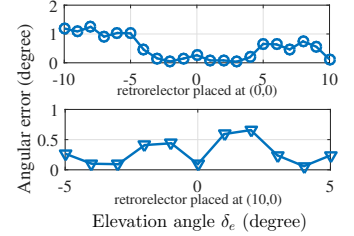


Fig. 23: Orientation error when the location is known

the devices. Although [4]–[6] are able to execute localization based on a single light source, they either necessitate camera to enable image processing [4], [5], or cannot localize static objects [6]. Utilizing a single light source, RETRO can achieve centimeter-level location accuracy and single-digit orientation error. A comparison with VLC-based localization systems is summarized in Table I.

VIII. CONCLUSION

In this paper, we propose and prototype RETRO, which to the best of our knowledge for the first time enables backward channel from the object to landmarks for VLC-based localization systems. Embracing all the advantages of VLC-based localization approach, such as high accuracy, orientation sensitivity, no interference to RF-based devices, RETRO is capable of utilizing any single unmodified light source to execute real-time tracking of location and orientation of any passive IoT device with ultra-low power and no computational capability at the devices. A set of extensive experimental results demonstrate that RETRO achieves remarkably good performance, and centimeter-level location error (i.e., less than 2 cm location error at 90% of the time) as well as up to 1° orientation error.

ACKNOWLEDGMENT

This work was supported in parts by NSF grants CNS-1617924 and EEC-1560131.

REFERENCES

- [1] S. Shao, A. Khreishah, M. Ayyash, M. B. Rahaim, H. Elgala, V. Jungnickel, D. Schulz, T. D. Little, J. Hilt, and R. Freund, “Design and analysis of a visible-light-communication enhanced WiFi system,” *IEEE/OSA JOCN*, vol. 7, no. 10, pp. 960–973, 2015.
- [2] L. Li, P. Hu, C. Peng, G. Shen, and F. Zhao, “Epsilon: A Visible Light Based Positioning System,” in *USENIX NSDI*, 2014, pp. 331–343.
- [3] Y.-S. Kuo, P. Pannuto, K.-J. Hsiao, and P. Dutta, “Luxapose: Indoor positioning with mobile phones and visible light,” in *ACM MobiCom*, 2014, pp. 447–458.
- [4] Z. Yang, Z. Wang, J. Zhang, C. Huang, and Q. Zhang, “Wearables can afford: Light-weight indoor positioning with visible light,” in *ACM MobiSys*, 2015, pp. 317–330.
- [5] C. Zhang and X. Zhang, “LiTell: Robust indoor localization using unmodified light fixtures,” in *ACM MobiCom*, 2016, pp. 230–242.
- [6] Z. Zhao, J. Wang, X. Zhao, C. Peng, Q. Guo, and B. Wu, “NaviLight: Indoor Localization and Navigation Under Arbitrary Lights,” in *IEEE INFOCOM*, 2017.
- [7] T. Li, C. An, Z. Tian, A. T. Campbell, and X. Zhou, “Human sensing using visible light communication,” in *ACM MobiCom*, 2015.
- [8] J. Li, A. Liu, G. Shen, L. Li, C. Sun, and F. Zhao, “Retro-VLC: Enabling battery-free duplex visible light communication for mobile and iot applications,” in *ACM HotMobile*, 2015, pp. 21–26.
- [9] S. Shao, A. Khreishah, and H. Elgala, “Pixelated VLC-backscattering for self-charging indoor IoT devices,” *IEEE Photonics Technology Letters*, vol. 29, no. 2, pp. 177–180, 2017.
- [10] A. Lundvall, F. Nikolajeff, and T. Lindström, “High performing micro-machined retroreflector,” *Optics express*, 2003.
- [11] Reflect-All, <https://reflect-all.com/>, [Online; accessed 2-May-2017].
- [12] D. A. Arnold, “Method of calculating retroreflector-array transfer functions,” *SAO Special Report*, vol. 382, 1979.
- [13] T. Komine and M. Nakagawa, “Fundamental analysis for visible-light communication system using LED lights,” *IEEE Transactions on Consumer Electronics*, vol. 50, no. 1, pp. 100–107, 2004.
- [14] Thorlabs, https://www.thorlabs.com/newgrouppage9.cfm?objectgroup_id=145, [Online; accessed 1-April-2017].
- [15] Refractive index database, <https://refractiveindex.info/?shelf=glass&book=BK7&page=SCHOTT>, [Online; accessed 2-May-2017].
- [16] Hamamatsu, https://www.hamamatsu.com/resources/pdf/ssd/s6801_etc_kpin1046e.pdf, [Online; accessed 1-April-2017].
- [17] B. Alsinglawi, M. Elkhodr, Q. V. Nguyen, U. Gunawardana, A. Maeder, and S. Simoff, “RFID Localisation for Internet of Things Smart Homes: A Survey,” *IJNC*, vol. 9, no. 1, 2017.
- [18] M. Kotaru, K. Joshi, D. Bharadia, and S. Katti, “Spotfi: Decimeter level localization using wifi,” in *ACM SIGCOMM*, 2015.
- [19] D. Vasisht, S. Kumar, and D. Katabi, “Decimeter-Level Localization with a Single WiFi Access Point,” in *USENIX NSDI*, 2016.
- [20] Apple Inc., <https://developer.apple.com/ibeacon/>, [Online; accessed 4-May-2017].
- [21] Decawave, <https://www.decawave.com/>, [Online; accessed 4-May-2017].